Title
High-pressure chemistry of hydrocarbons relevant to planetary interiors and inertial confinement fusion

Journal
Physics of Plasmas, 25(5)

ISSN
1070-664X

Authors
Kraus, D
Hartley, NJ
Frydrych, S
et al.

Publication Date
2018-05-01

DOI
10.1063/1.5017908

Peer reviewed

High-pressure chemistry of hydrocarbons relevant to planetary interiors and inertial confinement fusion

D. Kraus, N. J. Hartley, S. Frydrych, A. K. Schuster, K. Rohatsch, M. Rödel, T. E. Cowan, S. Brown, E. Cunningham, T. van Driel, L. B. Fletcher, E. Galtier, E. J. Gamboa, A. Laso Garcia, D. O. Gericke, E. Granados, P. A. Heimann, H. J. Lee, M. J. MacDonald, A. J. MacKinnon, E. E. McBride, I. Nam, P. Neumayer, A. Pak, A. Pelka, I. Prencipe, A. Ravasio, R. Redmer, A. M. Saunders, M. Schölmerich, M. Schörner, P. Sun, S. J. Turner, A. Zettl, R. W. Falcone, S. H. Glenzer, T. Döppner, and J. Vorberger

Citation: Physics of Plasmas **25**, 056313 (2018); doi: 10.1063/1.5017908

View online: https://doi.org/10.1063/1.5017908

View Table of Contents: http://aip.scitation.org/toc/php/25/5

Published by the American Institute of Physics

High-pressure chemistry of hydrocarbons relevant to planetary interiors and inertial confinement fusion

D. Kraus,[1,2,a)] N. J. Hartley,[1,3] S. Frydrych,[4,5] A. K. Schuster,[1] K. Rohatsch,[1] M. Rödel,[1] T. E. Cowan,[1] S. Brown,[6] E. Cunningham,[6] T. van Driel,[6] L. B. Fletcher,[6] E. Galtier,[6] E. J. Gamboa,[6] A. Laso Garcia,[1] D. O. Gericke,[7] E. Granados,[6] P. A. Heimann,[6] H. J. Lee,[6] M. J. MacDonald,[8,9] A. J. MacKinnon,[6] E. E. McBride,[6,10] I. Nam,[6] P. Neumayer,[11] A. Pak,[4] A. Pelka,[1] I. Prencipe,[1] A. Ravasio,[12] R. Redmer,[13] A. M. Saunders,[8] M. Schölmerich,[10] M. Schörner,[6,13] P. Sun,[6] S. J. Turner,[8] A. Zettl,[8] R. W. Falcone,[8,14] S. H. Glenzer,[6] T. Döppner,[4] and J. Vorberger[1]

[1]*Helmholtz-Zentrum Dresden-Rossendorf, Bautzner Landstrasse 400, 01328 Dresden, Germany*
[2]*Institute for Solid State and Materials Physics, Technische Universität Dresden, 01069 Dresden, Germany*
[3]*Open and Transdisciplinary Research Institute, Osaka University, Suita, Osaka 565-0871, Japan*
[4]*Lawrence Livermore National Laboratory, Livermore, California 94550, USA*
[5]*Institut für Kernphysik, Technische Universität Darmstadt, Schlossgartenstraße 9, 64289 Darmstadt, Germany*
[6]*SLAC National Accelerator Laboratory, Menlo Park, California 94309, USA*
[7]*CFSA, Department of Physics, University of Warwick, Coventry CV4 7AL, United Kingdom*
[8]*Department of Physics, University of California, Berkeley, California 94720, USA*
[9]*University of Michigan, Ann Arbor, Michigan 48109, USA*
[10]*European XFEL GmbH, Holzkoppel 4, 22869 Schenefeld, Germany*
[11]*GSI Helmholtzzentrum für Schwerionenforschung GmbH, Planckstraße 1, 64291 Darmstadt, Germany*
[12]*LULI, UMR7605, CNRS-CEA, Université Paris VI-Ecole Polytechnique, 91128 Palaiseau Cedex, France*
[13]*Institut für Physik, Universität Rostock, 18051 Rostock, Germany*
[14]*Lawrence Berkeley National Laboratory, Berkeley, California 94720, USA*

(Received 1 December 2017; accepted 8 May 2018; published online 23 May 2018)

Diamond formation in polystyrene $(C_8H_8)_n$, which is laser-compressed and heated to conditions around 150 GPa and 5000 K, has recently been demonstrated in the laboratory [Kraus *et al.*, Nat. Astron. **1**, 606–611 (2017)]. Here, we show an extended analysis and comparison to first-principles simulations of the acquired data and their implications for planetary physics and inertial confinement fusion. Moreover, we discuss the advanced diagnostic capabilities of adding high-quality small angle X-ray scattering and spectrally resolved X-ray scattering to the platform, which shows great prospects of precisely studying the kinetics of chemical reactions in dense plasma environments at pressures exceeding 100 GPa. https://doi.org/10.1063/1.5017908

I. INTRODUCTION

Matter states in the transition regime between condensed matter and hot, dense plasma exhibit temperatures of several thousand kelvins, corresponding to thermal energies approaching 1 eV. This is of the same order of magnitude as energies typically stored within chemical bonds. Thus, exotic chemical processes can occur, which are difficult to predict, as such states define the low-temperature end of the so-called warm dense matter (WDM) regime where most simple models break down.[1,2] However, these states of matter constitute the deep interiors of most planets in our solar system[3] and a steadily increasing number of extrasolar planets.[4,5] Thus, a precise characterization of WDM states is of paramount importance for understanding and predicting the properties of planets in our and other solar systems.

Particularly inside the giant planets of our solar system, several chemical processes are predicted to significantly influence the evolution and internal structure of these celestial bodies. One famous example is the transition from molecular hydrogen to metallic hydrogen, which may also be accompanied by hydrogen-helium de-mixing and subsequent helium precipitation inside Saturn.[6–9] On the other hand, it is predicted that the temperature inside of Jupiter may be too high to allow hydrogen-helium separation when hydrogen becomes metallic.[10–12]

The icy giants of our solar system are thought to contain a thick "ice" layer consisting of a mixture of water, methane, and ammonia between their gas atmospheres which are dominated by hydrogen and helium, and their rocky cores.[15–17] These ice layers are believed to facilitate the formation of very exotic microscopic structures, such as "superionic" water or ammonia.[13,14] The high-pressure and high-temperature environment may also result in chemical activity: methane is predicted to first dissociate and form polymeric hydrocarbon chains[19] before deeper towards the core, a full species separation into metallic hydrogen and carbon in the form of diamond may occur.[18,20–23] These diamond particles have a higher density than the surrounding ice fluid, and thus, the isolated carbon will precipitate towards the rocky core. Depending on

Note: Paper UI3 4, Bull. Am. Phys. Soc. **62**, 354 (2017).
[a)]Invited speaker.

the temperature at the boundary of the rocky core and the ice layer, either a layer of solid diamond or liquid carbon will form. Another possible precipitation process inside Neptune or Uranus may be the formation of ammonia hemihydrate $(H_2O)(NH_3)_2$ compounds that are predicted to remain stable up to 500 GPa.[24]

Chemical processes in the WDM regime are also of particular interest for several applications. In fact, phase separation of carbon and hydrogen is a potential concern for CH plastic ablator materials in inertial confinement fusion (ICF) capsule implosion experiments.[25] This phenomenon could lead to local density fluctuations, as local carbon and hydrogen clusters are forming, which could in turn seed hydrodynamic instabilities. Such instabilities, in particular ablation front Rayleigh-Taylor growth, were identified as one of the primary issues that led to reduced implosion performance during the National Ignition Campaign (NIC), where the first shock of the implosion drive created pressures of 100–200 GPa and temperatures of 0.6–1 eV in the ablator material.[26] While oxygen surface contaminants as well as the tent mounting of the fusion capsule inside the *Hohlraum* are likely candidates for increased amplitudes of the Rayleigh-Taylor-instability and thus of the reduced fusion performance, the possible effect of high-pressure chemistry during the first compression stages should not be neglected and needs to be investigated further. Studies with three-dimensional hydrodynamic simulations revealed that the surface roughness of the capsule is a major contribution for understanding the poor performance of the NIC campaign.[27,29] Therefore, the formation of spatial regions of higher and lower density due to carbon-hydrogen separation could potentially seed and enhance instability growth or mix of ablator material into the DT fuel in general and thus reduce the implosion performance.[28]

Hydrocarbons at extreme pressure and temperature conditions have been investigated by static compression techniques, mainly with resistively or laser-heated samples inside diamond anvil cells (DACs)[19,21,30] or dynamic compression experiments using gas guns,[31,32] explosives,[33] or high-energy laser pulses.[34] Both static and dynamic compression techniques have certain advantages and disadvantages: DACs allow for creating precise pressure and temperature states while providing excellent opportunities for time-integrated *in situ* measurements and sample recovery. On the other hand, DACs can only achieve pressure and temperature conditions up to a certain limit before the anvils will start to break. Moreover, it is very difficult to create chemically isolated systems, particularly for highly reactive materials such as hydrogen. Direct contact with the diamond anvils, metal gaskets, laser absorbants, and pressure standards can then significantly alter the results.

Dynamic compression experiments naturally create isolated systems due to the short time scale of the experiment (nanoseconds for laser-compression, microseconds for gas guns). It is however very difficult to determine the exact thermodynamic state of the sample. When applying a single shock compression wave, usually only pressure and density can precisely be inferred from the shock and particle velocities via the Rankine-Hugoniot relations. A reliable measurement of the temperature for dynamically compressed samples with temperatures of a few thousand kelvins remains very difficult. The uncertainties in the thermodynamic state increase for multiple shock compression and ramp compression since the simple relations for a single shock compression can no longer be applied and certain approximations for the transition states are required. However, such compression techniques are usually necessary to mimic the conditions deep inside planetary interiors, as a single shock to the desired pressure conditions will result in temperatures much higher than relevant for planetary interiors. By using multiple shocks or ramp compression, the entropy and thus the temperature increase can be reduced.[35,36] Moreover, direct *in situ* measurements of structural properties such as lattice structure or mesoscale structure remain very challenging for dynamic compression experiments.

In situ X-ray diffraction platforms for dynamically compressed samples exist at high-energy laser facilities, which have shown great results for structural phase transitions in mid- and higher-Z materials.[37] However, the materials that define the interiors of giant planets as well as ICF ablators consist of low-Z materials and scatter X-rays only weakly. Thus, X-ray sources of extreme brightness are required to obtain high-quality results. Recent experiments combining high-energy lasers with X-ray free electron lasers have started to revolutionize our understanding of dynamically compressed samples, including low-Z materials.[23,38–40]

In this article, we discuss a platform that allows for unprecedented studies of chemical processes in materials dynamically compressed to the edge of a dense plasma state. The combination of several X-ray techniques, particularly X-ray diffraction (XRD), spectrally resolved X-ray scattering (XRS), and small angle X-ray scattering (SAXS), in one experiment can provide unique insights into the chemical processes deep inside planetary interiors as well as within ablator materials during the first compression stage of inertial confinement fusion experiments. Moreover, we provide extended analysis and discussion of previously published XRD data in the context of first-principles simulations as well as additional data sets from laser-compressed polystyrene.

II. EXPERIMENTS

The discussed experiments were performed at the Matter in Extreme Conditions (MEC) endstation of the Linac Coherent Light Source (LCLS) of SLAC National Accelerator Laboratory (Fig. 1).[41–43] Solid samples of hydrocarbons are convenient initial materials to mimic the ice mixtures of icy giant planets in the laboratory.[32] While methane is present in the atmospheres of these planets, longer hydrocarbon chains are expected to form in the ice layers.[44] Therefore, plastic samples which have the additional advantage of being very easy to handle in the laboratory (compared to, e.g., cryogenic liquid methane) are chosen for our experiments.

The samples are compressed and heated using the pulsed high-energy drive laser available at MEC (15 J–32 J pulse

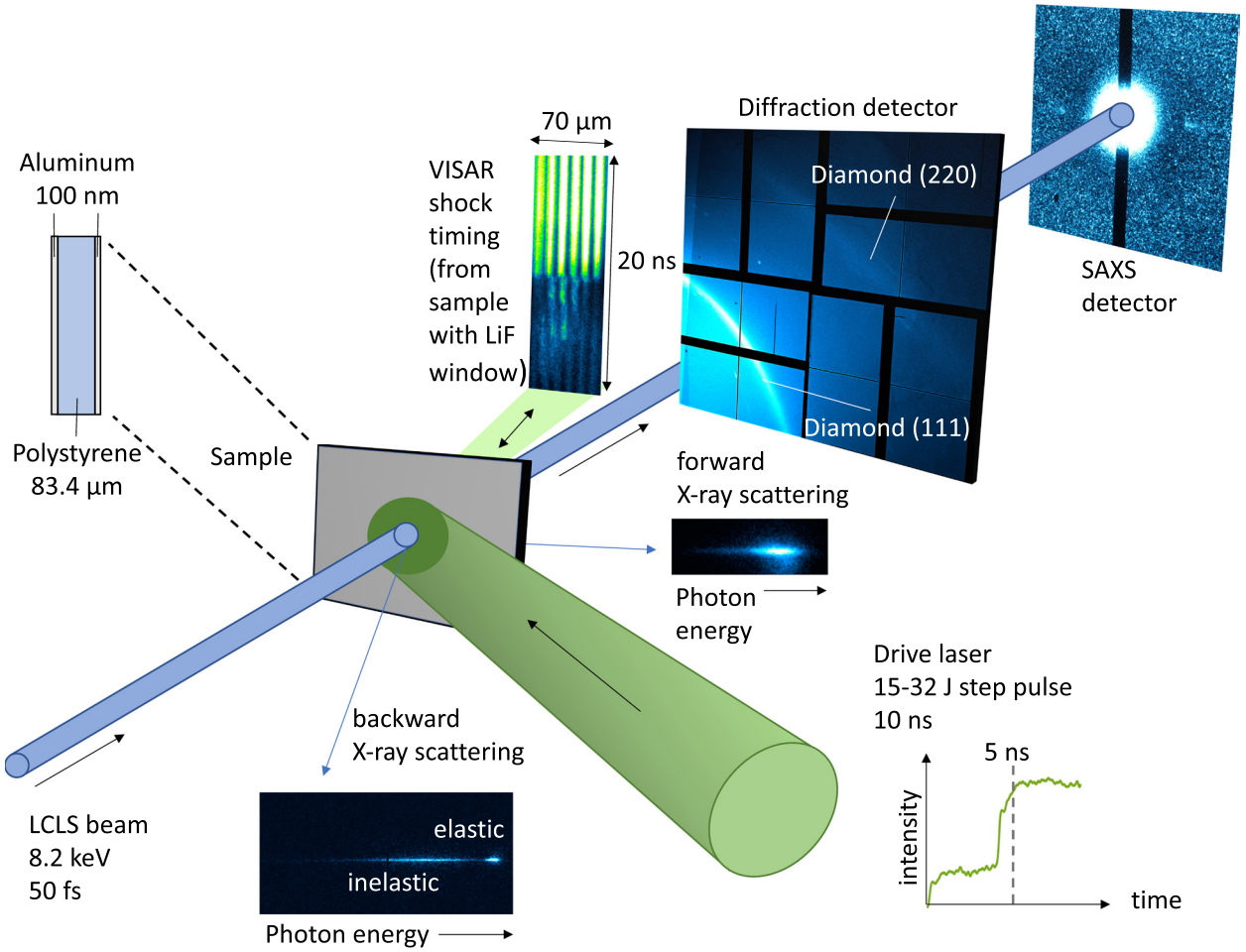

FIG. 1. Sketch of an experimental setup combining XRD, XRS, SAXS, and VISAR in one experiment. All diagnostic images shown demonstrate the high-quality single-shot data available at the MEC endstation of LCLS.

energy in 10 ns pulses focused to spot sizes of 150 μm–250 μm in diameter). Within a few picoseconds, the target surface is transferred into a rapidly expanding plasma state, which in turn drives a shock-compression wave into the cold material behind the ablation front.[45] For investigating conditions during the first compression stage of ICF, an ablator material, such as polystyrene $(C_8H_8)_n$, can be driven by a single shock-compression wave. In order to mimic planetary interiors, the sample can be compressed in two stages. This reduces the entropy increase in the overall compression process and thus the induced heat. For example, polystyrene will reach temperatures much higher than inside most planetary interiors when compressing to pressures above 100 GPa with a single shock. In our experiment, we used polystyrene samples with a thickness of 83.4 μm.

At MEC, the step pulse shapes required for the two-stage shock compression experiments can either be realized by delaying two flat-top pulses with respect to each other or using a pulse shaping system. The first option provides great flexibility for optimizing the exact delay of the second step and the relative intensity of the two steps. On the other hand, the pulse shaping option allows for quickly switching between shapes that have been saved to the system. However, setting up a new pulse shape, e.g., changing the delay between the steps or the relative intensity will require some time for optimization if the desired pulse shape has never been used before.

For optically transparent samples, like polystyrene and many other hydrocarbon materials, a thin aluminum front layer can serve as flash coating which prevents penetration of the drive laser onset into the transparent sample before an absorbing plasma is created at the front surface. Another thin aluminum layer at the sample rear side can be used to confirm the spatial alignment and timing of the X-ray pulse in respect to the shock dynamics. Aluminum absorbs the incident X-rays much more strongly than the hydrocarbon samples do. Thus, the aluminum layers can exhibit macroscopic responses to the X-ray irradiation, e.g., melting, while the structure of the hydrocarbon samples stays intact. The damage imprinted onto the Al layers can then be used as an alignment fiducial for spatially and temporally resolved optical diagnostics. We applied Al coatings of 100 nm thickness on both sides of the polystyrene samples.

The reflective metal layer also defines a surface that is useful for characterizing the shock dynamics with a Velocity Interferometer System for Any Reflector (VISAR).[46] Adding a window material, such as LiF, to the sample rear side, the velocity of the hydrocarbon-window interface can be traced. This serves as valuable tool for constraining density and pressure achieved inside the hydrocarbon sample.[23]

The compressed samples can simultaneously be probed by various X-ray diagnostic techniques. In our experiment, we applied a photon energy of 8.2 keV and with the high intensities of LCLS, all methods provide high-quality single-shot data. Thus, data accumulation is not required for characterizing a single sample condition. XRD is recorded by a 4×4 Cornell-SLAC hybrid Pixel Array Detector (CSPAD) detector[47] which covers diffraction angles from 18° to 85° (2θ). For XRS, two X-ray spectrometers in von-Hamos geometry, using $30 \times 32\,\mathrm{mm}^2$ highly annealed pyrolytic graphite (HAPG) crystals with a radius-of-curvature (ROC) of 51.7 mm as dispersive and imaging elements,[48] are placed at scattering angles of 17° and 123°, which corresponds to probed wave numbers at 1.23 Å^{-1} and 7.30 Å^{-1}, respectively. In each spectrometer, a 2×2 CSPAD is used as detector. The highest photon energy that can be resolved in 1st order reflection for the HAPG crystals is 8.2 keV for the applied spectrometers, which is the main reason why this photon energy is chosen for the experiment. In order to realize SAXS, a PIXIS XF 2048B X-ray detector was placed at 1460 mm downstream from the sample interaction point. This provides a coverage in reciprocal space from 0.005 Å^{-1} to 0.055 Å^{-1} (corresponding to scattering angles from 0.07° to 0.77°).

III. SIMULATIONS

Figure 2 illustrates numerical results of radiation-hydrodynamic simulations modeling the two-step compression process inside the described polystyrene samples using the hydrodynamic code package HELIOS-CR[49] with the SESAME 7592 equation of state (EOS) table for polystyrene.[50] Three different drive conditions are shown: "low drive" (1.42 TW/cm^2 followed by 6.04 TW/cm^2), "intermediate drive" (2.25 TW/cm^2 followed by 6.70 TW/cm^2), and "high drive" (2.67 TW/cm^2 followed by 7.55 TW/cm^2). The "intermediate drive" simulation has been tuned to reproduce the step pulse shape and the shock dynamics in the experiment (release and coalescence around 7.6 ns after the onset of the laser drive). Both for "low drive" and "high drive," the simulated drive intensities were then linearly scaled in relation to the laser energy measurement in the experiment.

For these adjusted drives, shock coalescence is no longer reached close to the sample rear side with a thickness that is optimal for the "intermediate drive." The "low drive" results in a coalescence of the two waves around mass coordinate 70 g/m^2, which produces a single shock that propagates from that point creating temperatures around 10 000 K. For the "high drive," the two compression waves no longer coalesce within the sample, since the first wave releases before the second wave can catch up. The amount of the sample material that is transferred to the hot plasma corona driving the shock wave is particularly visible in the temperature diagram. However, it accounts for only ~5% of the whole mass. Moreover, in the three-dimensional situation in the experiment, this amount will further be reduced compared to the hydrodynamic simulations, since the hot plasma will quickly escape to the sides of the spatial region heated by the drive laser. This is not modeled in the one-dimensional simulation geometry where the lateral extension of the drive laser spot is assumed to be infinitely large.

For modeling the microscopic properties of the sample conditions created, we set up density functional theory coupled to molecular dynamics (DFT-MD) simulations for the pressure and temperature reached by the intermediate drive (150 GPa, 5000 K). These simulations were performed using the package VASP,[51–54] where the electronic density was represented by a plane wave expansion with cutoff energy of $E_{\mathrm{cut}} = 1000$ eV. We used the Mermin formulation of DFT to optimize the Helmholtz free energy at a given temperature.[55] The electron-ion interaction was modeled using the projector augmented wave (PAW) approach, specifically the hard PAW pseudopotentials for carbon (four valence electrons) and hydrogen as provided with VASP.[56,57] The exchange-correlation potential was taken in generalized gradient approximation in Perdew-Burke-Ernzerhof parametrisation (GGA-PBE).[58,59] We generally sampled the Brillouin zone of the supercell at the Γ-point only. The electronic bands were populated using a Fermi distribution at the chosen temperature. We had to increase the number of computed electronic bands above the standard values in order to capture

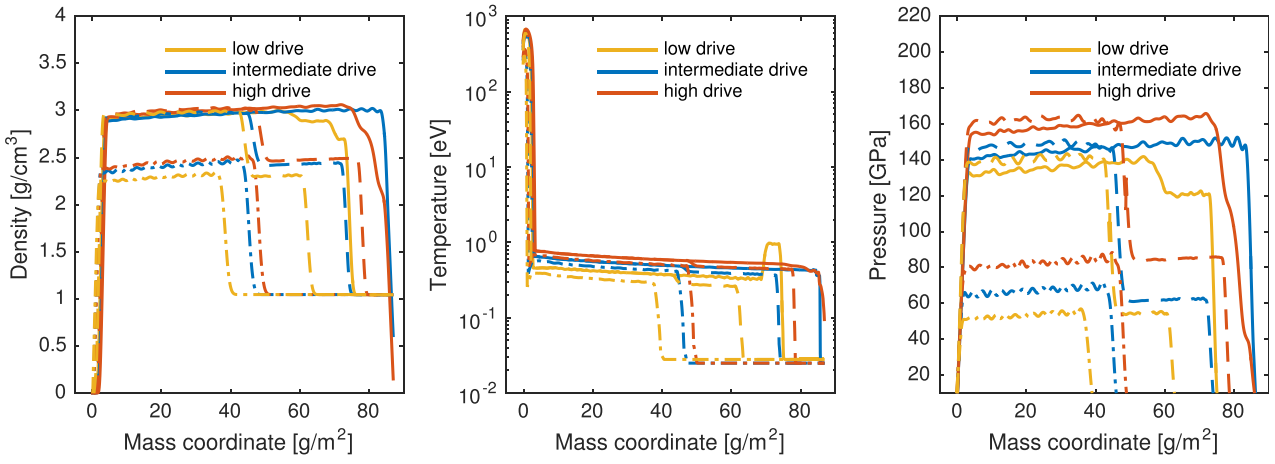

FIG. 2. Radiation hydrodynamic simulations of the three applied two-step compression drives. Dashed-dotted lines, dashed lines, and solid lines show the conditions 4.0 ns, 6.5 ns, and for 7.6 ns, after the drive laser impact, respectively. The laser is irradiating the sample from the left in all diagrams.

the tail of the Fermi distribution for all cases. The supercell contained approximately 500 atoms of carbon and hydrogen (ratio 1:1), whose movements according to Newton mechanics were calculated using the Hellman-Feynman forces derived from the electron densities of DFT in Born-Oppenheimer approximation. The time step was $t = 0.2$ fs and the DFT-MD run covers a time span of 20 ps. The ion temperature was controlled by a Nose-Hoover thermostat.[60] From the recorded MD coordinates, the ion structure and therefore the intensity of the elastic X-ray scattering in this multi-component system can be obtained.[61]

IV. RESULTS AND DISCUSSION

XRD raw data images recorded from polystyrene at ambient conditions and samples compressed by the three described compression pulse shapes are shown in Fig. 3. All depicted images of the driven samples were taken at very similar time delays (~7.5 ns) of the X-ray probe in relation to the onset of the compression drive. For all drives, the clear appearance of diamond diffraction features can be observed. Moreover, the Al signatures are reduced in comparison to the ambient samples and have completely disappeared for the "high drive."

Figure 4 illustrates diffraction lineouts extracted from the raw data images for polystyrene samples at ambient conditions as well as for the low, intermediate, and high drives that are shown in Fig. 3. For creating the lineouts, insensitive and overexposed regions of the detector are masked out for the azimuthal signal integration. Overall, the observed diffraction features are very compatible with the results of the hydrodynamic simulations. All laser drives show diamond formation after the second shock waves enters the sample.

For the "low drive," half of the aluminum signatures have been lost since the Al front layer is vaporized at the onset of the drive laser pulse while the back layer is still

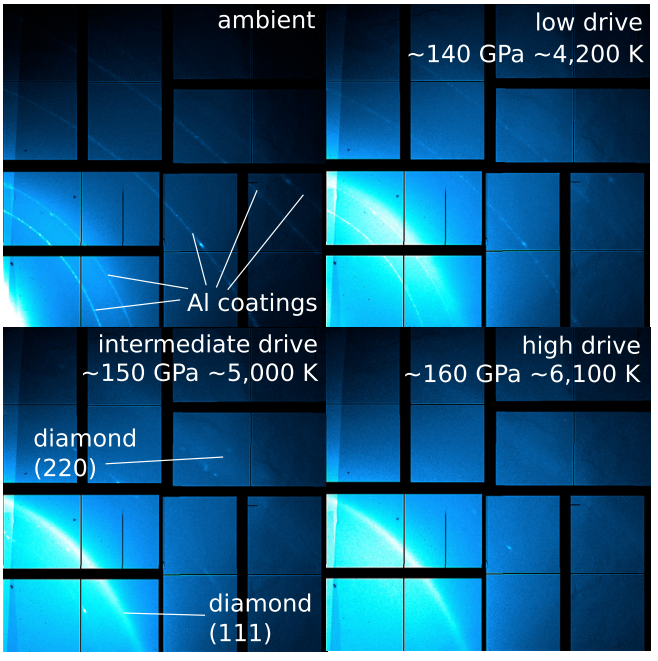

FIG. 3. X-ray diffraction raw data images for polystyrene at ambient conditions and the three different compression drives.

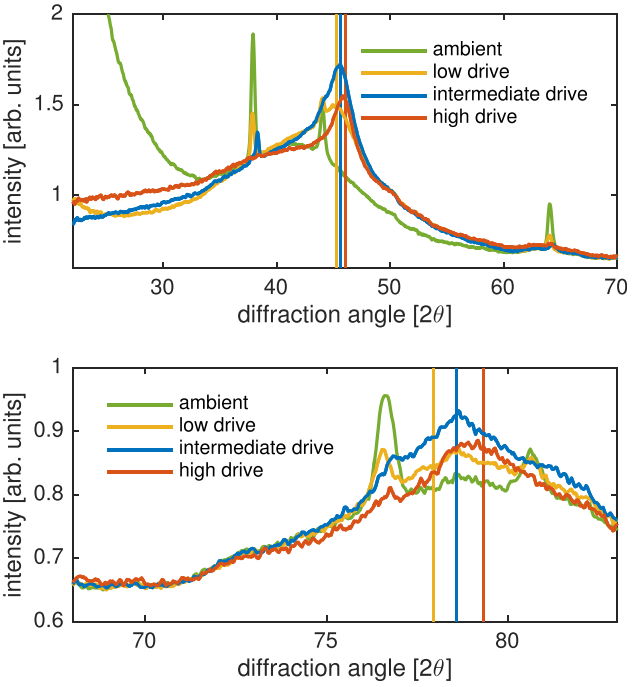

FIG. 4. Azimuthally integrated lineouts of the X-ray diffraction images shown in Fig. 3. Top: X-ray diffraction angles $2\theta = 22°$-$70°$. Bottom: X-ray diffraction angles $2\theta = 68°$-$83°$. The positions of the (111) and (220) diffraction peaks corresponding to the average diamond densities observed for the different drives ["low drive": (4.05 ± 0.07) g/cm^3, "intermediate drive": (4.14 ± 0.06) g/cm^3, and "high drive" (4.23 ± 0.05) g/cm^3], which were inferred from the more accurate positions of the (111) reflection, are marked by vertical lines [(111) in top diagram, (220) in bottom diagram].

intact at the time of probing, as neither shock wave has reached the rear side. For the "intermediate drive," the two shock waves are just reaching the rear surface and the corresponding Al diffraction signatures are right in the process of vanishing completely. This is underlined by the slight angular shift of the remaining Al diffraction peaks, which indicates compression of the Al layer for a short moment before it is vaporized upon release. For the "high drive," all Al signatures are gone since in this case both compression waves have already released at the rear side.

As the "intermediate drive" results in most of the sample being at conditions favoring diamond formation, the diamond diffraction signatures are more pronounced compared to the other drives. For the "low drive," there are some remnants of the strong signal at the smallest diffraction angles from the amorphous polystyrene at ambient conditions. For the "high drive," the signal at small diffraction angles is rising again compared to the "intermediate drive." This is due to contributions from low-density material created by the release of the compression waves. The positions of the diamond (111) diffraction peaks are slightly different for the varying drives, which is consistent with the different pressures achieved inside the samples. This feature is also visible for the (220) diffraction peaks, but less obvious due to the reduced signal quality at higher scattering angles. For comparison, Fig. 4 shows the position of the (111) and (220) diffraction peaks corresponding to the density inferred from the more accurate (111) reflection averaged separately for the three drives as vertical lines.

It should be noted that the observed relative variation of the diamond density for the different drives ("low drive": (4.05 ± 0.07) g/cm^3, "intermediate drive," (4.14 ± 0.06) g/cm^3 and "high drive" (4.23 ± 0.05) g/cm^3) is larger than the variation of the bulk density in the hydrodynamic simulations. This discrepancy may point to an inaccuracy of the applied CH EOS model, which does not include the phase separation reaction. However, a previously published[23] comparison with a state-of-the-art diamond EOS shows reasonable consistency for the overall pressure and temperature conditions obtained from the CH hydrodynamic simulations. Nevertheless, CH EOS models should certainly be revisited in this regime.

Figure 5 compares the XRD lineout of the "intermediate drive" to a synthetic XRD lineout extracted from a DFT-MD simulation of a carbon-hydrogen (1:1) mixture at ∼150 GPa and three temperature values of 4000 K, 5000 K, and 6000 K. This corresponds to the sample conditions expected for the "intermediate drive." As most of the sample is at relatively homogeneous conditions for this drive, when both compression waves coalesce at the sample rear side, the corresponding lineout is well-suited for the comparison with a simulation of a single pressure-temperature condition.

Overall, the simulated X-ray scattering lineouts provide reasonable agreement with the remaining liquid structure in the diffraction data recorded in the experiment. However, although hydrogen is found to be much more mobile than the carbon atoms, spontaneous carbon-hydrogen demixing and the particular formation of diamond structures cannot be observed in the simulation. This may be due to the limited time scales accessible by the applied computational methods, which typically allow for modeling processes not exceeding a few tens of picoseconds. While spontaneous demixing has been observed for hydrogen-helium mixtures by comparable simulations within 1 ps,[62] the heavier carbon atoms might increase demixing time scales in carbon-hydrogen mixtures. Another explanation may be the limited spatial scale due to the finite size of the simulation box. Unfortunately, both increasing spatial and time scales of these simulations up to regimes that reproduce the experimental scales are not feasible with contemporary computation resources.

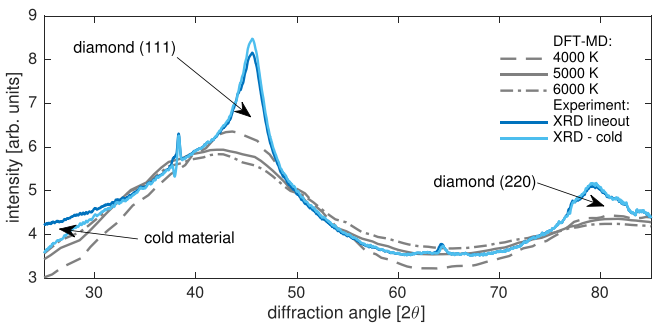

FIG. 5. Comparison of the experimental diffraction lineout for the "intermediate drive" and DFT-MD simulations of CH at a pressure of ∼150 GPa and varying temperatures. While the formation of diamond is not visible in the simulations, a better match at small diffraction angles is achieved after subtracting signal contributions of remaining cold material (XRD—cold).

Regarding the temperature variation, the simulations show best agreement with the remaining CH liquid for 5000 K, which is consistent with the hydrodynamic simulations. Only at small diffraction angles, the experimental lineout shows significantly larger values than suggested by all simulation runs. This discrepancy can be explained either by a small amount of remaining cold material, which provides strong diffraction at these diffraction angles (see Fig. 3), or low-density contributions of already released material. Indeed, a lineout, where a small fraction of ambient polystyrene diffraction has been subtracted, shows much better agreement with the simulations in this regime.

While the disagreement between the experimental and theoretical diffraction patterns are obvious for the case presented in Fig. 5, an even better comparison of experiment and theory will be possible when providing an absolute intensity scale for the experimental diffraction patterns. This will be particularly useful for testing the validity of simulations at conditions where the hydrocarbons remain in an amorphous or liquid state (e.g., as observed along the CH shock Hugoniot curve). Here, prominent solid diffraction features that allow for straightforward interpretations of the microscopic structure are not available. A possibility of providing a precise absolute scale for the X-ray diffraction lineouts is collecting spectrally resolved X-ray scattering data at fixed scattering angles that overlap with the angular regime covered by the XRD detector. A spectrometer at angles large enough that elastic scattering can clearly be distinguished from the inelastic Compton scattering should be the basis of the calibration, since the incoherent Compton scattering does then not depend on the crystalline or liquid structure of the sample. Usually, backscattering geometry is required to achieve such a clear separation of the two scattering features. A second spectrometer in forward scattering geometry, where the sensitivity has been cross-calibrated with the backscattering spectrometer, can then be set at an angle that overlaps with the angular coverage of the diffraction detector. The combination of these three instruments has been demonstrated at MEC and will allow to absolutely scale the diffraction images to the recorded Compton scattering intensity.

Figure 6 illustrates raw data lineouts of the applied spectrometers for a polystyrene sample at ambient conditions and a driven sample at the moment of approximate shock coalescence for the intermediate drive. For the larger scattering angle (123°), the elastic and inelastic scattering feature can clearly be distinguished. Due to little structural changes at large k, the ratio of elastic and inelastic scattering remains nearly unchanged from ambient conditions to the driven case. At small scattering angles, where the spectrum is largely dominated by elastic scattering, the situation is different. Here, the structural difference between ambient and driven samples results in a significant drop of the elastic scattering signal at 17°.

Another diagnostic method that will significantly enhance interpretations of the experiment is SAXS, which has a great potential to enable precise measurement of the nanodiamond size distribution created inside the plastic samples. This will provide valuable constraints on the kinetics of carbon-hydrogen demixing and diamond formation. So far,

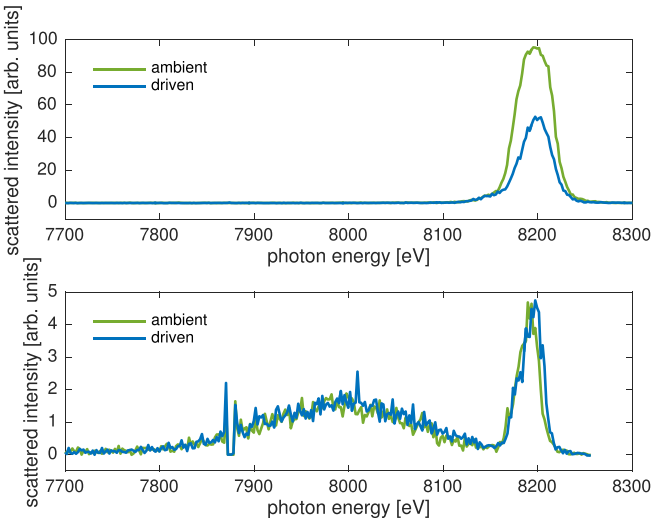

FIG. 6. Spectrally resolved X-ray scattering lineouts collected at 17° (top) and 123° (bottom).

we can only infer a lower limit of the nanodiamond size by applying the Scherrer formula[66] to the width of the XRD features. In this way, we obtain a lower limit of 3–4 nm diameter where the analysis ignores the fact that also lattice defects and spatial gradients can result in significant broadening of the diffraction features. Furthermore, SAXS will similarly be sensitive to the formation of liquid carbon clusters, which is highly interesting for plastic ablator materials used in ICF. The SAXS setup recently demonstrated at MEC and sketched in Fig. 1 has shown very promising single-shot sensitivity for providing additional *in situ* constraints on the nanodiamond size distribution.

Figure 7 shows SAXS raw data images for a polystyrene sample at ambient conditions and another image for the driven case taken at approximate shock coalescence. Both images apply the same color scale, which illustrates that the double-shock drive results in a strong increase in scattering signal in the larger k-regime of the detector. There is also a dim indication of ring-shaped darker region surrounding the central bright spot before the signal level again rises towards the detector edges. This type of feature can be expected for densely packed spheres, which is compatible with the formation of nanodiamonds as simultaneously observed by XRD.

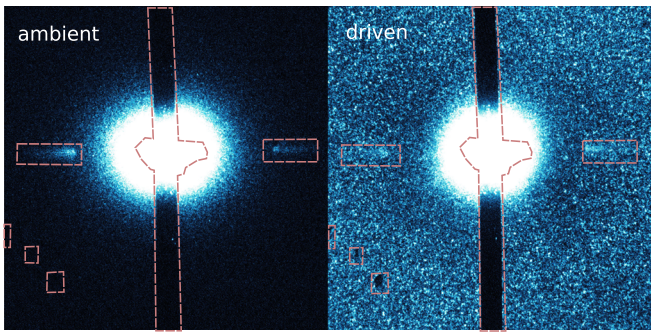

FIG. 7. SAXS raw data images from a polystyrene sample at ambient conditions and a driven sample at approximate shock coalescence. The dashed lines define the regions that are masked in the integration for obtaining the SAXS lineouts.

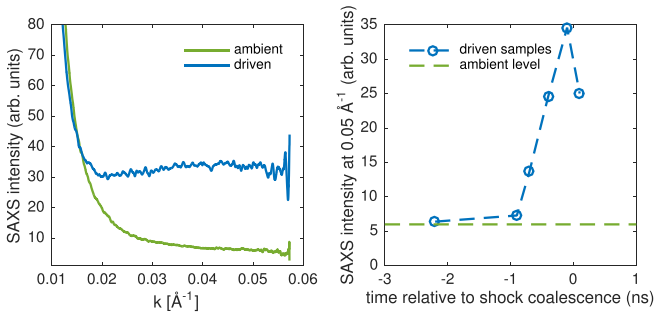

FIG. 8. Left: SAXS lineouts extracted from the images depicted in Fig. 7. Right: Time history of the SAXS feature connected to nanodiamond formation in relation to shock coalescence.

The signal minimum at $\sim 0.02\,\text{Å}^{-1}$ points to a particle size around ~ 5 nm, which is in very good agreement with the estimation obtained from the XRD peak width. For a detailed analysis, it needs to be considered that the shape of the SAXS signal is not only influenced by the particle size distribution but also by the volume fraction that the diamond particles fill inside the sample volume.

Figure 8 (left panel) depicts integrated lineouts obtained from the raw data images of Fig. 7. These greatly illustrate the signal increase at larger k due to the formation of nanodiamonds. The right panel of Fig. 8 shows the SAXS intensity at $0.05\,\text{Å}^{-1}$ for different timings in relation to shock coalescence. There is a strong and approximately linear increase in the last nanosecond before coalescence, which underlines that this feature clearly appears to be correlated to the formation of nanodiamonds while the second shock runs through the pre-compressed part of the sample and does not originate from other sources like hard X-rays created by the laser-plasma interaction.

V. CONCLUSIONS AND OUTLOOK

Using *in situ* XRD, our experiments have shown great capabilities for studying carbon-hydrogen demixing and diamond formation inside laser-compressed hydrocarbon samples on nanosecond timescales. From these results, we motivate experiments adding XRS and SAXS as standard diagnostics to the experimental platform. This allows for precisely studying the kinetics of hydrocarbon demixing and diamond formation in planetary environments as well as possible hydrocarbon demixing during the first stages of ICF implosion drive schemes involving plastic ablators. In particular for the latter case, a platform is required that can unambiguously judge whether carbon-hydrogen demixing already happens within the amorphous or liquid states along the shock Hugoniot curve. So far, our measurements only show that no diamonds are formed along the CH Hugoniot on nanosecond timescale. However, the presence of liquid carbon clusters cannot be excluded, since a significantly reduced diamond nucleation rate may prevent crystallization under these conditions[63] while short-time carbon bonds within the liquid[64,65] may help forming and sustaining carbon clusters.

In general, a better measurement of temperature will be crucial for further refinement of different models. However,

this quantity is very hard to determine precisely in the type of experiments described here. Future experiments should add streaked optical pyrometry (SOP), which is currently not a standard diagnostic tool at MEC. Moreover, high-precision measurements of the intensity ratio of the (111) and (220) diamond diffraction features may allow for constraining the temperature by fitting corresponding Debye-Waller-factors for the diamond lattice.

Future experiments will also aim to investigate solid plastics with different stoichiometries and compounds, e.g., polyethylene (CH_2), PMMA ($C_5H_8O_2$), PET ($C_{10}H_8O_4$), nylon ($C_6H_{11}NO$), etc. Using different compounds will aim for studying the effect of carbon concentration and the presence of oxygen or nitrogen on the kinetics of carbon-hydrogen demixing and diamond formation. Numerical studies indicate that both oxygen and nitrogen more support than prevent the formation of carbon clusters under these conditions,[22] but this still needs to be validated in an experiment. In order to best mimic the ice layers of Uranus and Neptune, liquid samples may be beneficial. With an ionic mixture of water, ammonia, and isopropanol, a H:O:C:N ratio of 28:7:4:1, which comes close to the predicted composition of Uranus, can be created. Therefore, this mixture is called "synthetic Uranus," and it has been extensively used in shock experiments with gas guns.[22] For laser experiments, liquid samples may either be realized by containing the liquid between a solid ablator material and a transparent VISAR window[40] or by liquid jets, which also allows for relatively simple use of cryogenic liquids (e.g., methane). The development of stable planar liquid cryogenic jets of several ten μm thickness is certainly challenging but there has been tremendous progress towards such a sample environment.[67]

In addition to the relevance of our results for planetary modeling and ICF, by showing the formation and release of nanodiamonds, our results identify a possible method to produce nanodiamonds from plastics for scientific and industrial applications. The occurrence of so-called detonation nanodiamonds in the soot of oxygen-deficient explosives has been known since the 1960s. Since the 1990s, this method has been applied as a commercial source of nanodiamonds.[68] Very similar diamond nanoparticles are evidently created in our laser-driven polystyrene samples. In fact, high-repetition rate laser systems (10 Hz or more) with comparable pulse energy as used for our measurements are nowadays readily available and the required double-stage shock compression can simply be realized by using two time-delayed drive lasers (as demonstrated in our experiment). Such laser irradiation of fast moving plastic films above a cooling medium like water could be a cleaner, easier to control and thus eventually cheaper method than the current industrial nanodiamond production using explosives. However, before such applications can be explored, effective recovery of nanodiamonds from laser-compressed plastics needs to be demonstrated. Such developments are now under way.

Finally, as the free hydrogen created by the carbon-hydrogen separation around 150 GPa and 5000 K is expected to be metallic,[69] the experimental platform described may also provide opportunities for further studies of this exotic state of matter that is thought to shape the magnetic fields of giant planets.

ACKNOWLEDGMENTS

This work was performed at the Matter at Extreme Conditions (MEC) instrument of LCLS, supported by the U.S. Department of Energy Office of Science, Fusion Energy Science under Contract No. SF00515. D.K., A.M.S., and R.W.F. acknowledge the support by the U.S. Department of Energy, Office of Science, Office of Fusion Energy Sciences, and by the National Nuclear Security Administration under Award Nos. DE-FG52–10NA29649 and DE-NA0001859. D.K., N.J.H., A.K.S., and K.R. were supported by the Helmholtz Association under VH-NG-1141. N.J.H. was supported by Kakenhi Grant No. 16K17846. SLAC HED was supported by DOE Office of Science, Fusion Energy Science, under FWP 100182. S.F. was supported by German Bundesministerium für Bildung und Forschung Project No. 05P15RDFA1. S.T. and A.Z. acknowledge support by the Air Force Office of Scientific Research under Award No. FA9550–14-1–0323 which provided for synthesis of low-density frameworks, and support from the Director, Office of Science, Office of Basic Energy Sciences, Materials Sciences and Engineering Division, of the U.S. Department of Energy under Contract No. DE-AC02–05-CH11231, within the sp2-Bonded Materials Program (KC2207) which provided for structural and chemical characterization. S.T. also received support from a National Science Foundation fellowship. R.R. acknowledges support from the DFG via the Research Unit FOR 2440. The work of A.P., S.F., and T.D. was performed under the auspices of the U.S. Department of Energy by Lawrence Livermore National Laboratory under Contract No. DE-AC52–07NA27344, and T.D. was supported by Laboratory Directed Research and Development (LDRD) Grant No. 18-ERD-033. R.W.F. acknowledges support of the University of California Center for Frontiers in High Energy Density Science.

[1]R. W. Lee, D. Kalantar, and J. Molitoris, "Warm dense matter: An overview," Report No. UCRL-TR-203844, Lawrence Livermore National Laboratory, 2004.
[2]*Frontiers and Challenges in Warm Dense Matter*, edited by F. Graziani, M. P. Desjarlais, R. Redmer, and S. B. Trickey (Springer Cham Heidelberg, New York, Dordrecht, London, 2014).
[3]T. Guillot, Science **286**, 72–77 (1999).
[4]D. C. Swift, J. H. Eggert, D. G. Hicks, S. Hamel, K. Caspersen, E. Schwegler, G. W. Collins, N. Nettelmann, and G. J. Ackland, Astrophys. J. **744**, 59 (2012).
[5]H. Rauer, C. Catala, C. Aerts, T. Appourchaux, W. Benz, A. Brandeker, J. Christensen-Dalsgaard, M. Deleuil, L. Gizon, M.-J. Goupil *et al.*, Exp. Astron. **38**, 249 (2014).
[6]E. E. Salpeter, Astrophys. J. **181**, L83 (1973).
[7]J. J. Fortney, Science **305**, 1414 (2004).
[8]R. Püstow, N. Nettelmann, W. Lorenzen, and R. Redmer, Icarus **267**, 323–333 (2016).
[9]M. Schöttler and R. Redmer, Phys. Rev. Lett. **120**, 115703 (2018).
[10]W. Lorenzen, B. Holst, and R. Redmer, Phys. Rev. Lett. **102**, 115701 (2009).
[11]M. A. Morales, C. Pierleoni, E. Schwegler, and D. M. Ceperley, Proc. Natl. Acad. Sci. **107**, 12799 (2010).
[12]J. M. McMahon, M. A. Morales, C. Pierleoni, and D. M. Ceperley, Rev. Mod. Phys. **84**, 1607 (2012).

[13]C. Cavazzoni, G. L. Chiarotti, S. Scandolo, E. Tosatti, M. Bernasconi, and M. Parinello, Science **283**, 44 (1999).
[14]M. Bethkenhagen, E. R. Meyer, S. Hamel, N. Nettelmann, M. French, L. Scheibe, C. Ticknor, L. A. Collins, J. D. Kress, J. J. Fortney *et al.*, Astrophys. J. **848**, 67 (2017).
[15]W. B. Hubbard, W. J. Nellis, A. C. Mitchell, S. S. Limaye, and P. C. McCandless, Science **253**, 648–651 (1991).
[16]R. Helled, J. D. Anderson, M. Podolak, and G. Schubert, Astrophys. J. **726**, 15 (2011).
[17]N. Nettelmann, K. Wang, J. J. Fortney, S. Hamel, S. Yellamilli, M. Bethkenhagen, and R. Redmer, Icarus **275**, 107–116 (2016).
[18]M. Ross, Nature **292**, 435–436 (1981).
[19]S. S. Lobanov, P.-N. Chen, X.-J. Chen, C.-S. Zha, K. D. Litasov, H.-K. Mao, and A. F. Goncharov, Nat. Commun. **4**, 2446 (2013).
[20]F. Ancilotto, G. L. Chiarotti, S. Scandolo, and E. Tosatti, Science **275**, 1288–1290 (1997).
[21]L. R. Benedetti, J. H. Nguyen, W. A. Caldwell, H. Liu, M. Kruger, and R. Jeanloz, Science **286**, 100–103 (1999).
[22]R. Chau, S. Hamel, and W. J. Nellis, Nat. Commun. **2**, 203 (2011).
[23]D. Kraus, J. Vorberger, A. Pak, N. J. Hartley, L. B. Fletcher, S. Frydrych, E. Galtier, E. J. Gamboa, D. O. Gericke, S. H. Glenzer *et al.*, Nat. Astron. **1**, 606–611 (2017).
[24]V. N. Robinson, Y. Wang, Y. Ma, and A. Hermann, Proc. Natl. Acad. Sci. **114**, 9003–9008 (2017).
[25]O. A. Hurricane, D. A. Callahan, D. T. Casey, P. M. Celliers, C. Cerjan, E. L. Dewald, T. R. Dittrich, T. Döppner, D. E. Hinkel, L. F. Berzak Hopkins *et al.*, Nature **506**, 343 (2014).
[26]J. Lindl, O. L. Landen, J. Edwards, E. Moses, and NIC Team, Phys. Plasmas **21**, 020501 (2014).
[27]T. R. Dittrich, O. A. Hurricane, D. A. Callahan, E. L. Dewald, T. Döppner, D. E. Hinkel, L. F. Berzak Hopkins, S. Le Pape, T. Ma, J. L. Milovich *et al.*, Phys. Rev. Lett. **112**, 055002 (2014).
[28]C. D. Orth, Phys. Plasmas **23**, 022706 (2016).
[29]D. S. Clark, C. R. Weber, J. L. Milovich, J. D. Salmonson, A. L. Kritcher, S. W. Haan, B. A. Hammel, D. E. Hinkel, O. A. Hurricane, O. S. Jones *et al.*, Phys. Plasmas **23**, 056302 (2016).
[30]H. Hirai, K. Konagai, T. Kawamura, Y. Yamamoto, and T. Yagi, Phys. Earth Planet. Inter. **174**, 242–246 (2009).
[31]W. J. Nellis, F. H. Ree, M. van Thiel, and A. C. Mitchell, J. Chem. Phys. **75**, 3055–3063 (1981).
[32]W. J. Nellis, D. C. Hamilton, and A. C. Mitchell, J. Chem. Phys. **115**, 1015–1019 (2001).
[33]N. R. Greiner, D. S. Phillips, J. D. Johnson, and F. Volk, Nature **333**, 440 (1988).
[34]M. A. Barrios, D. G. Hicks, T. R. Boehly, D. E. Fratanduono, J. H. Eggert, P. M. Celliers, G. W. Collins, and D. D. Meyerhofer, Phys. Plasmas **17**, 056307 (2010).
[35]Y. B. Zeldovic and Y. P. Raizer, *Physics of Shock Waves and High-Temperature Hydrodynamic Phenomena* (Academic, New York, 1966).
[36]D. C. Swift, R. G. Kraus, E. N. Loomis, D. G. Hicks, J. M. McNaney, and R. P. Johnson, Phys. Rev. E **78**, 066115 (2008).
[37]J. R. Rygg, J. H. Eggert, A. E. Lazicki, F. Coppari, J. A. Hawreliak, D. G. Hicks, R. F. Smith, C. M. Sorce, T. M. Uphaus, B. Yaakobi, and G. W. Collins, Rev. Sci. Instrum. **83**, 113904 (2012).
[38]D. Kraus, A. Ravasio, M. Gauthier, D. O. Gericke, J. Vorberger, S. Frydrych, J. Helfrich, L. B. Fletcher, G. Schaumann, B. Nagler *et al.*, Nat. Commun. **7**, 10970 (2016).
[39]U. Zastrau, E. J. Gamboa, D. Kraus, J. F. Benage, R. P. Drake, P. Efthimion, K. Falk, R. W. Falcone, L. B. Fletcher, E. Galtier *et al.*, Appl. Phys. Lett. **109**, 031108 (2016).
[40]A. E. Gleason, C. A. Bolme, E. Galtier, H. J. Lee, E. Granados, D. H. Dolan, C. T. Seagle, T. Ao, S. Ali, A. Lazicki *et al.*, Phys. Rev. Lett. **119**, 025701 (2017).
[41]M. Gauthier, L. B. Fletcher, A. Ravasio, E. Galtier, E. J. Gamboa, E. Granados, J. B. Hastings, P. Heimann, H. J. Lee, B. Nagler *et al.*, Rev. Sci. Instrum. **85**, 11E616 (2014).
[42]B. Nagler, B. Arnold, G. Bouchard, R. F. Boyce, R. M. Boyce, A. Callen, M. Campell, R. Curiel, E. Galtier, J. Garofoli *et al.*, J. Synchrotron Rad. **22**, 520–525 (2015).
[43]S. H. Glenzer, L. B. Fletcher, E. Galtier, B. Nagler, R. Alonso-Mori, B. Barbrel, S. B. Brown, D. A. Chapman, Z. Chen, C. B. Curry *et al.*, J. Phys. B: At. Mol. Opt. Phys. **49**, 092001 (2016).
[44]B. L. Sherman, H. F. Wilson, D. Weeraratne, and B. Militzer, Phys. Rev. B **86**, 224113 (2012).
[45]S. Eliezer, *The Interaction of High-Power Lasers with Plasmas* (Institute of Physics Publishing, Bristol and Philadelphia, 2002).
[46]L. M. Barker and R. E. Hollenbach, J. Appl. Phys. **43**, 4669–4675 (1972).
[47]S. Herrmann, S. Boutet, B. Duda, D. Fritz, G. Haller, P. Hart, R. Herbst, C. Kenney, H. Lemke, M. Messerschmidt *et al.*, Nucl. Instrum. Methods Phys. Res., Sect. A **718**, 550–553 (2013).
[48]U. Zastrau, A. Woldegeorgis, E. Förster, R. Loetzsch, H. Marschner, and I. Uschmann, J. Instrum. **8**, P10006 (2013).
[49]J. J. MacFarlane, I. E. Golovkin, and P. R. Woodruff, J. Quant. Spectrosc. Rad. Transfer **99**, 381–397 (2006).
[50]S. P. Lyon and J. D. Johnson, "SESAME: The Los Alamos National Laboratory equation of state database," LANL Report No. LA-UR-92-3407, 1992.
[51]G. Kresse and J. Hafner, Phys. Rev. B **47**, 558 (1993).
[52]G. Kresse and J. Hafner, Phys. Rev. B **49**, 14251 (1994).
[53]G. Kresse and J. Furthmüller, Comput. Mater. Sci. **6**, 15 (1996).
[54]G. Kresse and J. Furthmüller, Phys. Rev. B **54**, 11169 (1996).
[55]N. D. Mermin, Phys. Rev. **137**, A1441 (1965).
[56]P. E. Blöchl, Phys. Rev. B **50**, 17953 (1994).
[57]G. Kresse and D. Joubert, Phys. Rev. B **59**, 1758 (1999).
[58]J. P. Perdew, K. Burke, and M. Ernzerhof, Phys. Rev. Lett. **77**, 3865 (1996).
[59]J. P. Perdew, K. Burke, and M. Ernzerhof, Phys. Rev. Lett. **78**, 1396 (1997).
[60]S. Nose, Theor. Phys. Suppl. **103**, 1–46 (1991).
[61]K. Wünsch, J. Vorberger, G. Gregori, and D. O. Gericke, EPL **94**, 25001 (2011).
[62]W. Lorenzen, B. Holst, and R. Redmer, Phys. Rev. B **84**, 235109 (2011).
[63]L. M. Ghiringhelli, C. Valeriani, E. J. Meijer, and D. Frenkel, Phys. Rev. Lett. **99**, 055702 (2007).
[64]D. Kraus, J. Vorberger, D. O. Gericke, V. Bagnoud, A. Blazevic, W. Cayzac, A. Frank, G. Gregori, A. Ortner, A. Otten *et al.*, Phys. Rev. Lett. **111**, 255501 (2013).
[65]D. Kraus, J. Vorberger, J. Helfrich, D. O. Gericke, B. Bachmann, V. Bagnoud, B. Barbrel, A. Blazevic, D. C. Carroll, W. Cayzac *et al.*, Phys. Plasmas **22**, 056307 (2015).
[66]P. Scherrer, Göttinger Nachr. **2**, 98 (1918).
[67]L. B. Fletcher, U. Zastrau, E. Galtier, E. J. Gamboa, S. Goede, W. Schumaker, A. Ravasio, M. Gauthier, M. J. MacDonald *et al.*, Rev. Sci. Instrum. **87**, 11E524 (2016).
[68]V. N. Mochalin, O. Shenderova, D. Ho, and Y. Gogotsi, Nat. Nanotechnol. **7**, 11–23 (2012).
[69]T. Guillot and D. Gautier, Treatise Geophys. **10**, 439–464 (2007).